Small-Signal Models of Resonant Converter With Consideration of Different Duty-Cycle Control Schemes

Xin Li, *Member, IEEE*, Yiming Zhang, *Member, IEEE*, Shuxin Chen, *Student Member, IEEE*, Xin Zhang, *Senior Member, IEEE*, and Yi Tang, *Senior Member, IEEE*

***Abstract*—Duty-cycle control is a widely used control method of resonant converters. In this article, the existing model of duty-cycle controlled resonant converters is found to have discrepancy compared with the simulation and experimental results. The reason behind is investigated, showing the phase change in the output voltage of the inverter bridge caused by the duty-cycle perturbation was ignored in the existing model. The phase change law is highly dependent on the duty-cycle scheme used, which is further determined by the forms of the carriers and the switching sequences of the resonant converters. With this consideration, improved models of both full-bridge and half-bridge resonant converters with different duty-cycle control schemes are rederived. It is revealed that different duty-cycle control schemes lead to different phase curves of the duty-cycle-to-output-voltage transfer functions, therefore care should be taken when selecting the appropriate duty-cycle control scheme. In the end, a series-series compensated wireless power transfer system is built to verify the validity of the proposed models.**

***Index Terms*—Carriers, duty-cycle control, resonant converter, small-signal modeling, switching sequencies.**

I. Introduction

RESONANT converters have been demonstrated to be very suitable in high-frequency and high-efficiency power transfer. In recent years, various resonant topologies have been widely applied in the fields like data center power supply, electric vehicle charger, wireless power transfer (WPT), distributed power system in telecom, and network application among others [1]−[5].

The basic control method of resonant converters is variable frequency control. However, variable frequency control usually leads to large reactive power at light load, or a big switching frequency variation range when the input voltage range is wide. To solve this problem, the duty-cycle control has also been widely employed in many designs [6]–[11].

Dynamical models with good accuracy and a concise form are critical prerequisites for the analysis and dynamical control of resonant converters. Nevertheless, modeling resonant converters can be particularly challenging due to the high-frequency resonant mode operation, which renders the conventional state-space averaging technique no longer applicable [12]. For this purpose, some other modeling approaches suitable for resonant converters have been investigated. The discrete-time model or the sample-data model was proposed in [13] and [14]. The discrete-time model is known for its high accuracy. However, the derivation process involves solving a series of piecewise linear equations, and the result is represented by complicated matrix exponentials, which severely limits the use of the discrete-time model. Small-signal models based on state plane analysis and *dq*-transformation were proposed in [15] and [16], but this technique is mainly applicable to two-element resonant tanks. The idea that combines the time and frequency domain analyses provides some methods that are easy to understand and implement, for example, the dynamic phasor transform (DPT) technique [17], [18] and the generalized state space averaging (GSSA) method [19], [20], and the extended describing function (EDF) method in [21] and [22]. The methodologies of the three methods are similar, that is, decomposing the switching ripple of each variable in the resonant tank into two independent variables with dc operating points, so as to obtain a linearized small-signal model around the dc operating points. Although the ways of the decomposition are different, the derived models by the three methods, e.g., [17]–[22], are essentially identical. In addition, these approaches can also offer the corresponding equivalent circuits of the models [21]. Compared with the form of state-space representation, the equivalent circuit is simpler and more straightforward. Recently, some reduced-order equivalent circuits have been proposed in [23] and [24], further facilitating the analysis and the closed-loop design of resonant converters.

To date, the DPT, GSSA, and EDF methods are among the most popular modeling approaches, with which, the models for both variable frequency control and duty-cycle control of many resonant converters have been established. The obtained models by the three methods for varying frequency control

Manuscript received November 2, 2020; revised March 10, 2021; accepted April 28, 2021. Date of publication May 11, 2021; date of current version July 30, 2021. This work was part of the research program of Maritime Research Between Singapore (Singapore Maritime Institute) and Norway (Research Council of Norway) under Project SMI-2019-MA-02, which was supported by the Singapore Maritime Institute. Recommended for publication by Associate Editor M. Ordonez. *(Corresponding author: Yi Tang.)*

Xin Li, Yiming Zhang, Shuxin Chen, and Yi Tang are with the School of Electrical and Electronic Engineering, Nanyang Technological University, Singapore 639798, Singapore (e-mail: li-xin@ntu.edu.sg; zhangym07@gmail.com; chen1095@e.ntu.edu.sg; yitang@ntu.edu.sg).

Xin Zhang is with the College of Electrical Engineering, Zhejiang University, Hangzhou 310027, China (e-mail: zhangxin_ieee@zju.edu.cn).

Color versions of one or more figures in this article are available at https://doi.org/10.1109/TPEL.2021.3079343.

Digital Object Identifier 10.1109/TPEL.2021.3079343

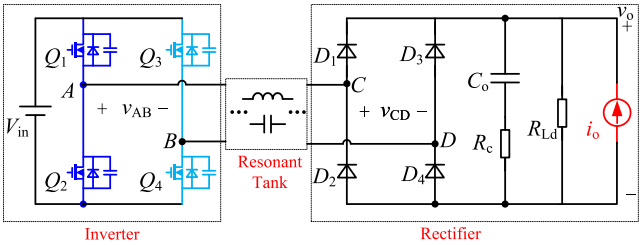

Fig. 1. General structure of a typical resonant converter.

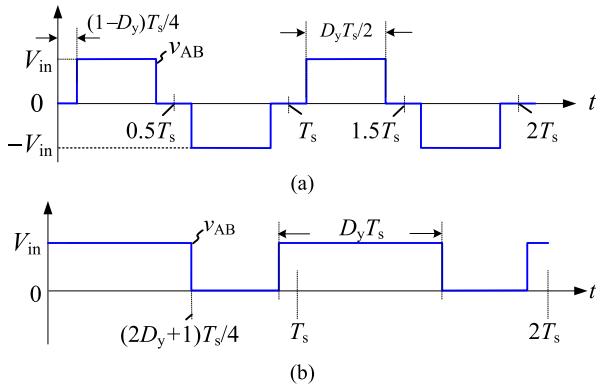

Fig. 2. v_{AB} and its fundamental harmonic component in (a) full-bridge inverter and (b) half-bridge inverter.

and input voltage control show very good consistency with the simulation and experiment. However, it is found that the existing models for duty-cycle control using the three methods, e.g., [25]−[29] are not accurate. Significant errors are observed at certain duty-cycles. Besides, categorized by the forms of carriers and the switching sequences, there are various duty-cycle control schemes, but they are also found to have different models, which cannot be explained by the existing models as it has nothing to do with how the duty-cycle is realized.

This article studies the reason behind this phenomenon and rederives an improved model with better accuracy for duty-cycle controlled resonant converters. Both the full-bridge and half-bridge structures of the inverter bridges are considered. This article is organized as follows. Section II has a brief review of the existing modeling procedure of the EDF method. Sections III and IV propose the improved models using the EDF method for full-bridge and half-bridge resonant converters, respectively. Section V gives a detailed discussion of the proposed model. Section VI provides the experimental results of a series-series (*S*-*S*) compensated WPT system to validate the proposed model. Finally, Section VII concludes this article.

II. Brief Review of the Existing Model of Resonant Converters

Fig. 1 is the general structure of a typical resonant converter. It consists of an inverter bridge, a resonant tank, and a rectifier tank. The inverter can be full-bridge or half-bridge structures. In the full-bridge structure, there are four switches (Q_1–Q_4); in the half-bridge structure, there are two switches (Q_1, Q_2), and point B is connected to the ground. The resonant tank is composed of inductors, capacitors, and an optional isolation transformer. Different combinations of the inductors and capacitors constitute diverse resonant topologies. In Fig. 1, v_{in} is the input voltage, v_{AB} is the output voltage of the inverter, v_o is the output voltage, i_o is the external output current, C_o is the output capacitor, and R_c is the equivalent series resistance of C_o, R_{Ld} is the load resistance. The switching angular frequency is ω_s and the switching period is T_s.

In the EDF method, using Fourier transform, the state variable in the resonant tank x can be decomposed to

$$x = \sum_{n=0}^{+\infty} \left(x_{(ns)} \sin(n\omega_s t) + x_{(nc)} \cos(n\omega_s t) \right) \tag{1}$$

where $x_{(ns)}$ and $x_{(nc)}$ are, respectively, the coefficients of the $\sin(n\omega_s t)$ term and the $\cos(n\omega_s t)$ term of x.

Similarly, as the excitation of the resonant tank, v_{AB} can also be decomposed to

$$v_{AB}(t) = \sum_{n=0}^{+\infty} \left(v_{AB(ns)} \sin(n\omega_s t) + v_{AB(nc)} \cos(n\omega_s t) \right). \tag{2}$$

Fig. 2(a) shows the waveforms of v_{AB} in full-bridge resonant converters, which is a pure ac quasi-square, the Fourier series of which is

$$v_{AB}(t) = \sum_{n=1}^{\infty} \frac{4v_{in}}{n\pi} \sin\left(n\frac{\pi}{2}\right) \sin\left(\frac{nd_y\pi}{2}\right) \sin(n\omega_s t). \tag{3}$$

Based on (3), the expressions of $v_{AB(ns)}$ and $v_{AB(nc)}$ ($n = 1$, 2, 3, …) are readily solved as

$$v_{AB(ns)} = \frac{4v_{in}}{n\pi} \sin\left(n\frac{\pi}{2}\right) \sin\left(\frac{nd_y\pi}{2}\right) \tag{4a}$$

$$v_{AB(nc)} = 0. \tag{4b}$$

Similarly, Fig. 2(b) shows the waveforms of v_{AB} in half-bridge resonant converters, and the corresponding Fourier series is

$$v_{AB}(t) = v_{in}d_y + \sum_{n=1}^{\infty} \frac{2v_{in}}{n\pi} \sin(nd_y\pi) \cos\left(n\omega_s t - \frac{n\pi}{2}\right). \tag{5}$$

The deduced $v_{AB(ns)}$ and $v_{AB(nc)}$ are

$$v_{AB(ns)} = \frac{2v_{in}}{n\pi} \sin\left(\frac{n\pi}{2}\right) \sin(nd_y\pi) \tag{6a}$$

$$v_{AB(nc)} = \frac{2v_{in}}{n\pi} \cos\left(\frac{n\pi}{2}\right) \sin(nd_y\pi). \tag{6b}$$

Note that $x_{(ns)}$, $x_{(nc)}$, $v_{AB(ns)}$, and $v_{AB(nc)}$ are dc values in the steady state but will oscillate at the perturbation frequency around the dc values when perturbed. Therefore, replacing x, v_{AB} with $x_{(ns)}$, $x_{(nc)}$, $v_{AB(ns)}$, $v_{AB(nc)}$, and using harmonic

balance, a new state equation with a fixed dc operation point can be obtained [21].

To further obtain a linearized model, small-signal perturbations are introduced, i.e.,

$$\begin{aligned} d_{\rm y} &= D_{\rm y} + \hat{d}_{\rm y} \\ v_{\rm in} &= V_{\rm in} + \hat{v}_{\rm in} \\ i_{\rm o} &= 0 + \hat{i}_{\rm o} \end{aligned} \tag{7}$$

where the symbols with the first letter capitalized are the steady-state components of the variables, while the symbols with caps are the small-signal components of the variables.

Substituting of (7) into (4) and (6) and then performing linearization lead to the small-signal expressions of $\hat{v}_{{\rm AB}(ns)}$ and $\hat{v}_{{\rm AB}(nc)}$. For the full-bridge inverter, we have

$$\hat{v}_{{\rm AB}(ns)} = \frac{4}{n\pi}\sin\left(n\frac{\pi}{2}\right)\sin\left(\frac{nD_{\rm y}\pi}{2}\right)\hat{v}_{\rm in} + 2V_{\rm in}\sin\left(\frac{n\pi}{2}\right)\cos\left(\frac{nD_{\rm y}\pi}{2}\right)\hat{d}_{\rm y} \tag{8a}$$

$$\hat{v}_{{\rm AB}(nc)} = 0. \tag{8b}$$

For the half-bridge inverter, we have

$$\hat{v}_{{\rm AB}(ns)} = \frac{2}{n\pi}\sin\left(\frac{n\pi}{2}\right)\sin\left(nD_{\rm y}\pi\right)\hat{v}_{\rm in} + 2V_{\rm in}\sin\left(\frac{n\pi}{2}\right)\cos\left(nD_{\rm y}\pi\right)\hat{d}_{\rm y} \tag{9a}$$

$$\hat{v}_{{\rm AB}(nc)} = \frac{2}{n\pi}\cos\left(\frac{n\pi}{2}\right)\sin\left(nD_{\rm y}\pi\right)\hat{v}_{\rm in} + 2V_{\rm in}\cos\left(\frac{n\pi}{2}\right)\cos\left(nD_{\rm y}\pi\right)\hat{d}_{\rm y}. \tag{9b}$$

Finally, a complete linearized small-signal model can be obtained as

$$\frac{d}{dt}\begin{bmatrix}\hat{\mathbf{x}}_{\rm s}\\ \hat{\mathbf{x}}_{\rm c}\\ \hat{v}_{\rm Co}\end{bmatrix} = \mathbf{A}_{\rm ss}\begin{bmatrix}\hat{\mathbf{x}}_{\rm s}\\ \hat{\mathbf{x}}_{\rm c}\\ \hat{v}_{\rm Co}\end{bmatrix} + \mathbf{B}_{\rm ss}\begin{bmatrix}\hat{v}_{\rm in}\\ \hat{d}_{\rm y}\\ \hat{i}_{\rm o}\end{bmatrix} \tag{10}$$

$$\hat{v}_{\rm o} = \mathbf{C}_{\rm ss}\begin{bmatrix}\hat{\mathbf{x}}_{\rm s}\\ \hat{\mathbf{x}}_{\rm c}\\ \hat{v}_{\rm Co}\end{bmatrix} + \mathbf{D}_{\rm ss}\begin{bmatrix}\hat{v}_{\rm in}\\ \hat{d}_{\rm y}\\ \hat{i}_{\rm o}\end{bmatrix} \tag{11}$$

where $\mathbf{A}_{\rm ss}$, $\mathbf{B}_{\rm ss}$, $\mathbf{C}_{\rm ss}$, and $\mathbf{D}_{\rm ss}$ are the coefficients matrices of the small-signal model.

Equations (10) and (11) are the widely used standard EDF-based model of a duty-cycle controlled resonant converter [21], from which, the input-voltage-to-output-voltage transfer function $G_{\rm vg}(s)$, the duty-cycle-to-output-voltage transfer function $G_{\rm vd}(s)$, the output impedance transfer function $Z_{\rm o}(s)$ can be extracted as

$$G_{\rm vg}(s) = \left[\mathbf{C}_{\rm ss}(s\mathbf{I}-\mathbf{A}_{\rm ss})^{-1}\mathbf{B}_{\rm ss}+\mathbf{D}_{\rm ss}\right]\begin{bmatrix}1&0&0\end{bmatrix}^{\rm T} \tag{12a}$$

$$G_{\rm vd}(s) = \left[\mathbf{C}_{\rm ss}(s\mathbf{I}-\mathbf{A}_{\rm ss})^{-1}\mathbf{B}_{\rm ss}+\mathbf{D}_{\rm ss}\right]\begin{bmatrix}0&1&0\end{bmatrix}^{\rm T} \tag{12b}$$

$$Z_{\rm o}(s) = \left[\mathbf{C}_{\rm ss}(s\mathbf{I}-\mathbf{A}_{\rm ss})^{-1}\mathbf{B}_{\rm ss}+\mathbf{D}_{\rm ss}\right]\begin{bmatrix}0&0&1\end{bmatrix}^{\rm T}. \tag{12c}$$

In this article, it is found that $G_{\rm vg}(s)$ and $Z_{\rm o}(s)$ by the existing model coincide with the experimental data very well, however, $G_{\rm vd}(s)$ is found to be inaccurate in certain circumstances. Different duty-cycle control schemes are found to have different models, which cannot be reflected by the existing $G_{\rm vd}(s)$. The reason lies in the handling of $v_{\rm AB}$ under duty-cycle perturbation, which will be reinvestigated in the following using the EDF method. It is worth noting that the theoretical analysis can be extended to the GSSA method and DPT method, as discussed in Appendix A.

III. Small-Signal Model for Full-Bridge Inverter

A. Classification of Different Phase-Shift Control Schemes for Full-Bridge Structure

In full-bridge resonant converters, the duty-cycle control is usually implemented by phase-shift (PS) between the leading-leg and the lagging leg. There are two commonly used shapes of carriers, namely the sawtooth carrier (SC) and the triangle carrier (TC), which leads to six different PS control schemes, as shown in Fig. 3. Without loss of generality, the leg composed of Q_1 and Q_2 is fixed, while the phase of the leg composed of Q_3 and Q_4 is shifted according to the modulation signal.

In Fig. 3(a), the rising type SC is used. In this case, Q_1 and Q_2 constitute the lagging leg, Q_3 and Q_4 constitute the leading leg. At the instants when the duty-cycle modulation signal $v_{\rm mod}$ intersects the carrier $v_{\rm car}$, Q_3 and Q_4 toggle the states to implement PS.

In Fig. 3(b), the falling type SC is used. In this case, Q_1 and Q_2 constitute the leading leg, Q_3 and Q_4 constitute the lagging leg. At the instants when $v_{\rm mod}$ intersects $v_{\rm car}$, Q_3 and Q_4 toggle the states to realize PS.

In Fig. 3(c), the TC is used. Q_1 and Q_2 constitute the lagging leg, Q_3 and Q_4 constitute the leading leg. $v_{\rm mod}$ compares with $v_{\rm car}$ during the rising period of $v_{\rm car}$ to determine the turn-ON instant of Q_3. After half of the switching cycle, Q_4 turns ON naturally.

In Fig. 3(d), the TC is used. In this case, Q_1 and Q_2 are the leading leg, Q_3 and Q_4 are the lagging leg. $v_{\rm mod}$ compares with $v_{\rm car}$ during the falling period of $v_{\rm car}$ to determine the turn-ON instant of Q_3. After half of the switching cycle, Q_4 turns ON naturally.

Fig. 3(e) and (f) are respectively the dualities of Fig. 3(c) and (d) by exchanging the positions of Q_1 and Q_2 as well as Q_3 and Q_4.

Note that for TC, there are two forms of the leading-leg PS and lagging-leg PS. For ease of presentation, Fig. 3(c) and (e) are, respectively, named Form 1 and Form 2 of TC leading-leg PS; Fig. 3(d) and (f) are, respectively, named Form 1 and Form 2 of TC lagging-leg PS. Although there are a variety of PS control schemes, they can be summarized into two categories, i.e., the leading-leg PS [see Fig. 3(a), (c), and (e)] and the lagging-leg PS [see Fig. 3(b), (d), and (f)]. Fourier transform will be performed on $v_{\rm AB}$ to investigate the effect of different duty-cycle control schemes.

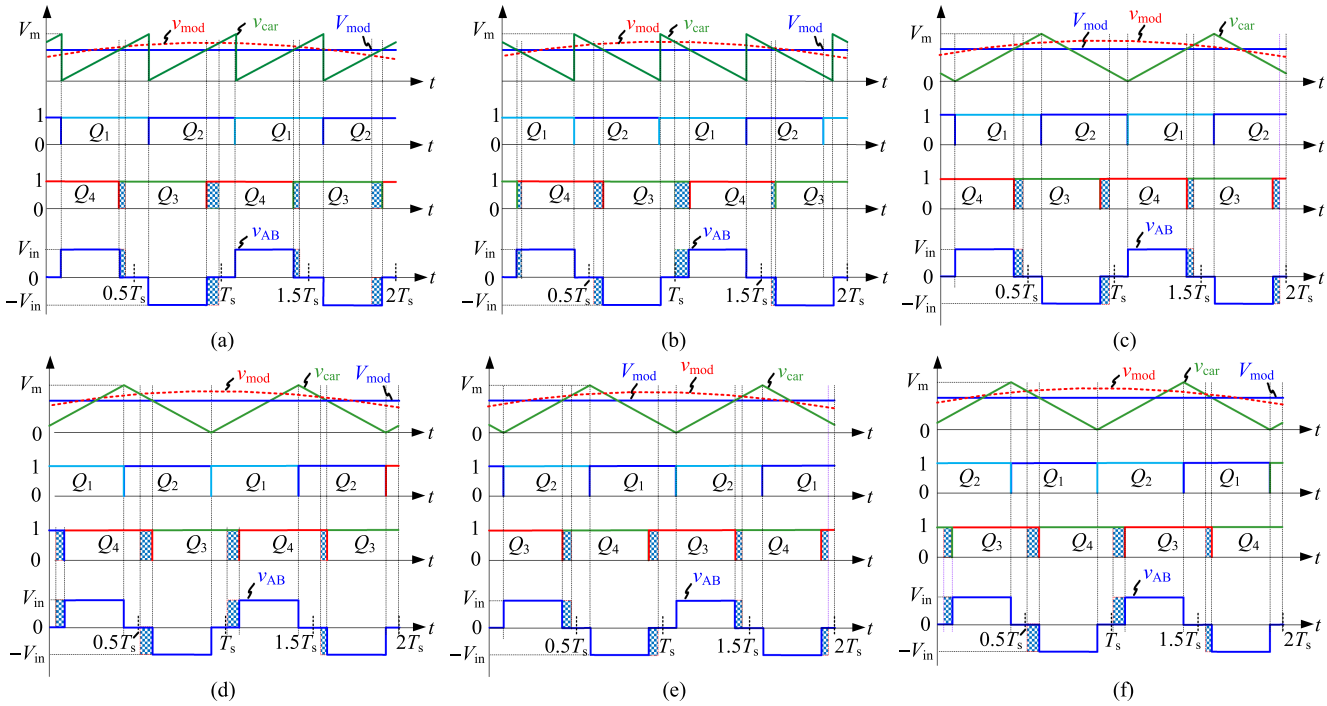

Fig. 3. Different PS control schemes for full-bridge inverter. (a) SC leading-leg PS. (b) SC lagging-leg PS. (c) TC leading-leg PS, Form 1. (d) TC lagging-leg PS, Form 1. (e) TC leading-leg PS, Form 2. (f) TC lagging-leg PS, Form 2.

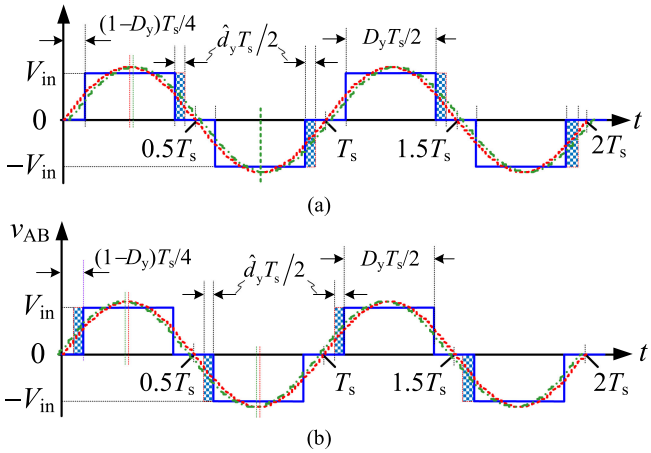

Fig. 4. Summarized two kinds waveforms of $v_{\rm AB}$ by different PS schemes. (a) Leading-leg PS. (b) Lagging-leg PS.

B. Small-Signal Model of the Full-Bridge Inverter

The waveforms of $v_{\rm AB}$ by leading-leg PS and lagging-leg PS are illustrated in Fig. 4(a) and (b), respectively. To keep consistent with the existing models, the zero time of $v_{\rm AB}$ is also selected at the zero-crossing point of its fundamental component in steady state as Fig. 2 does. As can be seen in Fig. 4, when there is a perturbation in the duty-cycle, the zero-crossing point of $v_{\rm AB}$ will change accordingly. Considering this, for leading-leg PS, the expression of $v_{\rm AB}$ in one switching cycle becomes

$$v_{\rm AB}(t) = \begin{cases} V_{in} \text{if} (1-D_{\rm y})T_{\rm s}/4 < t < (1+D_{\rm y})T_{\rm s}/4 + \hat{d}_{\rm y}T_{\rm s}\big/2 \\ 0 \text{if} (1+D_{\rm y})T_{\rm s}/4 + \hat{d}_{\rm y}T_{\rm s}\big/2 < t < (3-D_{\rm y})T_{\rm s}/4 \\ -V_{in} \text{if} (3-D_{\rm y})T_{\rm s}/4 < t < (3+D_{\rm y})T_{\rm s}/4 + \hat{d}_{\rm y}T_{\rm s}\big/2 \\ 0 \text{if} (3+D_{\rm y})T_{\rm s}/4 + \hat{d}_{\rm y}T_{\rm s}\big/2 < t < (5-D_{\rm y})T_{\rm s}/4. \end{cases} \tag{13}$$

Please note that, since $G_{\rm vg}(s)$ and $Z_{\rm o}(s)$ have no the inaccuracy issue as $G_{\rm vg}(s)$ does, $\hat{v}_{\rm in}$ and $\hat{i}_{\rm o}$ are not considered in (13).

Performing Fourier transform on (13) yields

$$v_{\rm AB}(t) = \sum_{n=1}^{\infty} \frac{4V_{\rm in}}{n\pi} \sin\left(n\frac{\pi}{2}\right) \sin\left(\frac{nd_{\rm y}\pi}{2}\right) \sin\left(n\omega_s t - \frac{n\pi}{2}\hat{d}_{\rm y}\right). \tag{14}$$

Comparing (14) with (3), it can be found that the amplitude of each harmonic is the same, but the phase of the nth harmonic lags the existing result by $\frac{n\pi}{2}\hat{d}_{\rm y}$.

Using $d_{\rm y} = D_{\rm y} + \hat{d}_{\rm y}$, (14) is simplified to be

$$\begin{aligned} v_{\rm AB}(t) = \sum_{n=1}^{\infty} \tfrac{4V_{\rm in}}{n\pi} \sin\left(\tfrac{n\pi}{2}\right) \cdot \\ \left[\sin\left(\tfrac{nD_{\rm y}\pi}{2}\right)\cos\left(\tfrac{n\hat{d}_{\rm y}\pi}{2}\right) + \cos\left(\tfrac{n\pi D_{\rm y}}{2}\right)\sin\left(\tfrac{n\hat{d}_{\rm y}\pi}{2}\right)\right] \\ \left[\sin\left(n\omega_s t\right)\cos\left(\tfrac{n\pi}{2}\hat{d}_{\rm y}\right) - \cos\left(n\omega_s t\right)\sin\left(\tfrac{n\pi}{2}\hat{d}_{\rm y}\right)\right]. \end{aligned} \tag{15}$$

When $\hat{d}_{\rm y} << 1$, the following approximations hold true

$$\cos\left(\frac{n\hat{d}_{\rm y}}{2}\pi\right) \approx 1, \sin\left(\frac{n\hat{d}_{\rm y}}{2}\pi\right) \approx \frac{n\hat{d}_{\rm y}}{2}\pi \tag{16}$$

Substituting (16) into (15), the small-signal component $\hat{v}_{\rm AB}(t)$ is solved as

$$\hat{v}_{\rm AB}(t) = \sum_{n=1}^{\infty}\left[2V_{\rm in}\sin\left(\frac{n\pi}{2}\right)\cos\left(\frac{n\pi D_{\rm y}}{2}\right)\hat{d}_{\rm y}\sin\left(n\omega_s t\right) - 2V_{\rm in}\sin\left(\frac{n\pi}{2}\right)\sin\left(\frac{nD_{\rm y}\pi}{2}\right)\hat{d}_{\rm y}\cos\left(n\omega_s t\right)\right]. \tag{17}$$

from which, $\hat{v}_{{\rm AB}(ns)}$ and $\hat{v}_{{\rm AB}(nc)}$ for leading-leg PS control are readily obtained as

$$\hat{v}_{{\rm AB}(ns)} = 2V_{\rm in}\sin\left(\frac{n\pi}{2}\right)\cos\left(\frac{n\pi D_{\rm y}}{2}\right)\hat{d}_{\rm y} \tag{18a}$$

$$\hat{v}_{{\rm AB}(nc)} = -2V_{\rm in}\sin\left(\frac{n\pi}{2}\right)\sin\left(\frac{nD_{\rm y}\pi}{2}\right)\hat{d}_{\rm y}. \tag{18b}$$

Similarly, for the case of lagging-leg PS control in Fig. 4(b), the expression of $v_{\rm AB}$ in time domain is

$$v_{\rm AB}(t) = \begin{cases} V_{in} \text{ if } (1-D_{\rm y})T_{\rm s}/4 - \hat{d}_{\rm y}T_{\rm s}\Big/2 < t < (1+D_{\rm y})T_{\rm s}/4 \\ 0 \text{ if } (1+D_{\rm y})T_{\rm s}/4 < t < (3-D_{\rm y})T_{\rm s}/4 - \hat{d}_{\rm y}T_{\rm s}\Big/2 \\ -V_{in} \text{ if } (3-D_{\rm y})T_{\rm s}/4 - \hat{d}_{\rm y}T_{\rm s}\Big/2 < t < (3+D_{\rm y})T_{\rm s}/4 \\ 0 \text{ if } (3+D_{\rm y})T_{\rm s}/4 < t < (5-D_{\rm y})T_{\rm s}/4 - \hat{d}_{\rm y}T_{\rm s}\Big/2. \end{cases} \tag{19}$$

Performing Fourier transform on (19), it is obtained as

$$v_{\rm AB}(t) = \sum_{n=1}^{\infty}\frac{4V_{\rm in}}{n\pi}\sin\left(n\frac{\pi}{2}\right)\sin\left(\frac{nd_{\rm y}\pi}{2}\right)\sin\left(n\omega_s t + \frac{n\pi}{2}\hat{d}_{\rm y}\right). \tag{20}$$

In this case, the phase of the *n*th harmonic is found to lead the existing result in (3) by $\frac{n\pi}{2}\hat{d}_{\rm y}$.

Using the same method as leading-leg PS control, the expressions of $\hat{v}_{{\rm AB}(ns)}$ and $\hat{v}_{{\rm AB}(nc)}$ for lagging-leg PS control are derived as

$$\hat{v}_{{\rm AB}(ns)} = 2V_{\rm in}\sin\left(\frac{n\pi}{2}\right)\cos\left(\frac{n\pi D_{\rm y}}{2}\right)\hat{d}_{\rm y} \tag{21a}$$

$$\hat{v}_{{\rm AB}(nc)} = 2V_{\rm in}\sin\left(\frac{n\pi}{2}\right)\sin\left(\frac{nD_{\rm y}\pi}{2}\right)\hat{d}_{\rm y}. \tag{21b}$$

The gains from $\hat{d}_{\rm y}$ to $\hat{v}_{{\rm AB}(ns)}$and $\hat{v}_{{\rm AB}(nc)}$ are respectively defined as $G_{{\rm AB}(ns)}$ and $G_{{\rm AB}(nc)}$, whose expressions by the existing model can be obtained from (8), while the results by the proposed model can be obtained from (18) and (21) accordingly. Since the resonant tank is tuned close to the resonant frequency that allows mainly the fundamental frequency in most resonant converters, only the case when $n = 1$ is considered here, but the theoretical analysis in this article still applies when considering the third harmonic or higher harmonics as well [30]–[34]. The expressions of $G_{\rm AB(1s)}$ and $G_{\rm AB(1c)}$ corresponding to different PS control schemes are concluded and tabulated in Table I. According to Table I , the expressions of $G_{\rm AB(1s)}$ by the proposed model are consistent with those of the existing model. However, $G_{\rm AB(1c)}$ is no longer zero as the existing model predicted, and has different expressions for leading-leg PS and lagging-leg PS controls.

TABLE I
EXPRESSIONS OF $G_{\rm AB(1s)}$ AND $G_{\rm AB(1c)}$ FOR FULL-BRIDGE INVERTER

Models	$G_{\rm AB(1s)}$	$G_{\rm AB(1c)}$
Existing model	$2V_{\rm in}\cos\left(\frac{D_{\rm y}}{2}\pi\right)$	0
Proposed Model for leading-leg PS	$2V_{\rm in}\cos\left(\frac{D_{\rm y}}{2}\pi\right)$	$-2V_{\rm in}\sin\left(\frac{D_{\rm y}}{2}\pi\right)$
Proposed Model for lagging-leg PS	$2V_{\rm in}\cos\left(\frac{D_{\rm y}}{2}\pi\right)$	$2V_{\rm in}\sin\left(\frac{D_{\rm y}}{2}\pi\right)$

TABLE II
EXPRESSIONS OF $G_{\rm AB(1s)}$ AND $G_{\rm AB(1c)}$ FOR HALF-BRIDGE INVERTER

Models	$G_{\rm AB(1s)}$	$G_{\rm AB(1c)}$
Existing model	$2V_{\rm in}\cos\left(D_{\rm y}\pi\right)$	0
Proposed Model for trailing-edge modulation	$2V_{\rm in}\cos\left(D_{\rm y}\pi\right)$	$-2V_{\rm in}\sin\left(D_{\rm y}\pi\right)$
Proposed Model for leading-edge modulation	$2V_{\rm in}\cos\left(D_{\rm y}\pi\right)$	$2V_{\rm in}\sin\left(D_{\rm y}\pi\right)$
Proposed Model for dual-edge modulation	$2V_{\rm in}\cos\left(D_{\rm y}\pi\right)$	0

TABLE III
PARAMETERS OF THE *S-S* COMPENSATED WPT SYSTEM

Parameters	Values	Parameters	Values
$V_{\rm in}$	20 V	R_2	0.3 Ω
$f_{\rm s}$	125 kHz	M	9.6 μH
L_1	41 μH	$C_{\rm o}$	4.7 μF
C_1	50 nF	$R_{\rm Ld}$	15.5 Ω
R_1	0.5 Ω	$R_{\rm c}$	1 mΩ
L_2	39 μH	$H_{\rm v}$	0.1
C_2	50 nF	$V_{\rm m}$	1

IV. SMALL-SIGNAL MODEL FOR HALF-BRIDGE INVERTER

A. Classification of Different Duty-Cycle Control Schemes for Half-Bridge Inverter

In the half-bridge inverter, the carrier for the duty-cycle control can also be SC and TC. Fig. 5(a)–(c) gives the corresponding waveforms of the half-bridge inverter with different carriers.

In Fig. 5(a), the rising type SC is used. In this case, the instant when the modulation signal $v_{\rm mod}$ intersects the carrier $v_{\rm car}$ determines the turn-OFF instant of Q_1. As the trailing edge of $v_{\rm AB}$ is modulated, it is also called trailing-edge modulation [35].

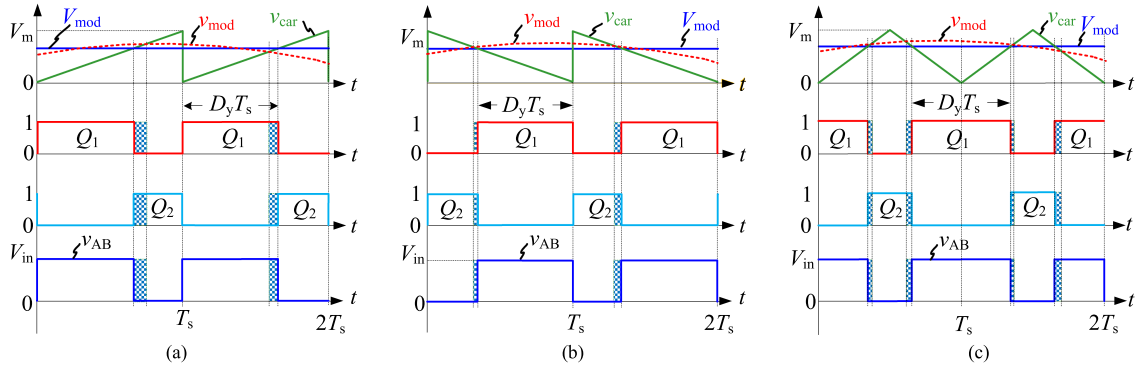

Fig. 5. Different duty-cycle modulation schemes for the half-bridge inverter. (a) SC trailing-edge modulation. (b) SC leading-edge modulation. (c) TC dual-edge modulation.

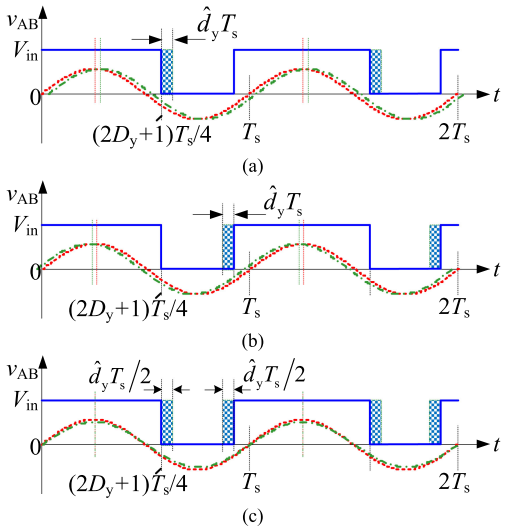

Fig. 6. Three kinds of waveforms of $v_{\rm AB}$ and the fundamental harmonic components by different duty-cycle control schemes. (a) Trailing-edge modulation. (b) Leading-edge modulation. (c) Dual-edge modulation.

In Fig. 5(b), the falling type SC is used. In this case, the instant when $v_{\rm mod}$ intersects the carrier $v_{\rm car}$ determines the turn-ON instant of Q_1. As the leading edge of $v_{\rm AB}$ is modulated, it is also called leading edge modulation [35].

In Fig. 5(c), the TC is used. In this case, both the turn-ON and turn-OFF instants of Q_1 are regulated by $v_{\rm mod}$. This is also named as dual-edge modulation [36].

In conclusion, for the half-bridge inverter, the duty-cycle control schemes can be divided into three categories, which will be derived respectively.

B. Small-Signal Model of the Half-Bridge Inverter

The waveforms of $v_{\rm AB}$ by the three duty-cycle control schemes are illustrated in Fig. 6.

For trailing-edge modulation in Fig. 6(a), the expression of $v_{\rm AB}$ under duty-cycle perturbation in one switching cycle is

$$v_{\rm AB}(t) = \begin{cases} 0 \text{ if } (2D_{\rm y}+1)T_{\rm s}/4 + \hat{d}_{\rm y}T_{\rm s} < t < (5-2D_{\rm y})T_{\rm s}/4 \\ V_{in} \text{ if } (5-2D_{\rm y})T_{\rm s}/4 < t < (2D_{\rm y}+5)T_{\rm s}/4 + \hat{d}_{\rm y}T_{\rm s}. \end{cases} \tag{22}$$

Performing Fourier transform on (22) leads to

$$v_{\rm AB}(t) = V_{\rm in}d_{\rm y} + \sum_{n=1}^{\infty} \frac{2V_{\rm in}}{n\pi} \sin(nd_{\rm y}\pi) \cos\left(n\omega_s t - \frac{n\pi}{2} - n\hat{d}_{\rm y}\pi\right). \tag{23}$$

After that, linearizing (23) results in the following expressions of $\hat{v}_{{\rm AB}(ns)}$ and $\hat{v}_{{\rm AB}(nc)}$ for trailing-edge modulation

$$\hat{v}_{{\rm AB}(ns)} = 2V_{\rm in} \sin\left(nD_{\rm y}\pi + \frac{n\pi}{2}\right)\hat{d}_{\rm y} \tag{24a}$$

$$\hat{v}_{{\rm AB}(nc)} = 2V_{\rm in} \cos\left(nD_{\rm y}\pi + \frac{n\pi}{2}\right)\hat{d}_{\rm y}. \tag{24b}$$

Similarly, for leading-edge modulation in Fig. 6(b), the expression of $v_{\rm AB}$ in one switching cycle is

$$v_{\rm AB}(t) = \begin{cases} 0 \text{ if } (2D_{\rm y}+1)T_{\rm s}/4 < t < (5-2D_{\rm y})T_{\rm s}/4 - \hat{d}_{\rm y}T_{\rm s} \\ V_{in} \text{ if } (5-2D_{\rm y})T_{\rm s}/4 - \hat{d}_{\rm y}T_{\rm s} < t < (2D_{\rm y}+5)T_{\rm s}/4. \end{cases} \tag{25}$$

After Fourier transform, we can obtain that

$$v_{\rm AB}(t) = V_{\rm in}d_{\rm y} + \sum_{n=1}^{\infty} \frac{2V_{\rm in}}{n\pi} \sin(nd_{\rm y}\pi) \cos\left(n\omega_s t - \frac{n\pi}{2} + n\hat{d}_{\rm y}\pi\right) \tag{26}$$

from which, the expressions of $\hat{v}_{{\rm AB}(ns)}$and $\hat{v}_{{\rm AB}(nc)}$for leading-edge modulation are found to be

$$\hat{v}_{{\rm AB}(ns)} = -2V_{\rm in} \sin\left(nD_{\rm y}\pi - \frac{n\pi}{2}\right)\hat{d}_{\rm y} \tag{27a}$$

$$\hat{v}_{{\rm AB}(nc)} = 2V_{\rm in} \cos\left(nD_{\rm y}\pi - \frac{n\pi}{2}\right)\hat{d}_{\rm y}. \tag{27b}$$

For dual-edge modulation in Fig. 6(c), the expression of $v_{\rm AB}$ in one switching cycle is

$$v_{\rm AB}(t) = \begin{cases} 0 \text{ if } (2D_{\rm y}+1)T_{\rm s}/4 + \hat{d}_{\rm y}T_{\rm s} < t < (5-2D_{\rm y})T_{\rm s}/4 - \hat{d}_{\rm y}T_{\rm s} \\ V_{in} \text{ if } (5-2D_{\rm y})T_{\rm s}/4 - \hat{d}_{\rm y}T_{\rm s} < t < (2D_{\rm y}+5)T_{\rm s}/4 + \hat{d}_{\rm y}T_{\rm s}. \end{cases} \tag{28}$$

The Fourier transform of (28) as well as the derived $\hat{v}_{{\rm AB}(ns)}$ and $\hat{v}_{{\rm AB}(nc)}$ are found to be completely consistent with the existing result, namely (5), (9) in Section II.

All the expressions of $G_{\rm AB(1s)}$ and $G_{\rm AB(1c)}$ for half-bridge inverter by the existing model and the proposed model are collected and list in Table II, where we can see that the expressions of $G_{\rm AB(1s)}$ are identical in all duty-cycle control schemes and

are consistent with the existing model, while the expressions of $G_{\mathrm{AB(1c)}}$ are different. The existing model agrees with the proposed model only when dual-edge modulation is used.

V. Comparison and Discussion

Based on the analysis above, this article makes a modification to the standard modeling procedures of the EDF method in [21]. When modeling a resonant converter with duty-cycle control, we need to select the corresponding $G_{\mathrm{AB(1s)}}$ and $G_{\mathrm{AB(1c)}}$ from Tables I or II according to the actual duty-cycle control scheme to get the expressions of $v_{\mathrm{AB(1s)}}$ and $v_{\mathrm{AB(1c)}}$. Except for this, other procedures in [21] remain completely unchanged. Besides, the modified transfer function of $G_{\mathrm{vd}}(s)$ is still expressed as (12b) except that some elements related to the $\hat{d}_{\mathrm{y}}$ in matrix $\mathbf{B}_{\mathrm{ss}}$ are changed. Other transfer functions, such as $G_{\mathrm{vg}}(s)$, $Z_{\mathrm{o}}(s)$, etc. are completely unaffected.

A. Physical Insights of the Proposed Model

The proposed model exhibits distinct characteristics from the existing model, which will be interpreted here by acquiring the physical insights.

As shown in Figs. 4 and 6, the actual v_{AB} is a square wave or a quasi-square wave. After injecting duty-cycle perturbation into the modulation signal, the pulsewidth of v_{AB} changes. In the full-bridge structure, no matter the leading-leg PS or the lagging-leg PS is adopted, the pulsewidth expands along just one side of the center line of v_{AB} in each half switching cycle, causing the center line to move synchronously. For the two PS schemes, the center line moves in opposite directions. Considering the peak of the fundamental harmonic of v_{AB} is always aligned with the center line, therefore both the amplitude and phase of the fundamental harmonic component of v_{AB} would change with the perturbation of duty-cycle, which is well described by the proposed model with the nonzero $G_{\mathrm{AB(1c)}}$. The fundamental harmonic components of v_{AB} before and after imposing duty-cycle perturbation are depicted in Fig. 4 (red dotted line and green dash-dotted line respectively) to show the small phase difference.

The same explanation also applies to the leading-edge modulation and trailing-edge modulation in the half-bridge structure. However, for the dual-edge modulation, the pulsewidth of v_{AB} is symmetrically increased on both sides of the center line after the injection of the duty-cycle perturbation, which does not affect the phase of the fundamental harmonic component.

Furthermore, for leading-leg PS and lagging-leg PS or leading-edge modulation and trailing-edge modulation, the phase of the fundamental component of v_{AB} changes in the opposite direction, therefore the signs of $G_{\mathrm{AB(1c)}}$ are also opposite.

With regard to the existing model, nevertheless, the Fourier transform is in fact performed on the steady-state waveform of v_{AB}, instead of the actual wave after duty-cycle perturbation. Since the phase of the steady-state fundamental harmonic component of v_{AB} is fixed and has nothing to do with the duty-cycle [see (3) and (5)], therefore the information of the phase change is ignored by the existing model, which inevitably leads to errors.

B. Case Study

To further demonstrate the proposed models, the *S-S* compensated WPT system is taken as an example to illustrate this issue. Fig. 7 gives the topology of the *S-S* compensated WPT system, where $L_{1(2)}$ and $C_{1(2)}$ are the self-inductances and the compensation capacitors for the transmitting side and receiving side respectively, M is the mutual inductance. $i_{1(2)}$ is the current of the transmitting coil and the receiving coil, $v_{1(2)}$ is the voltage of $C_{1(2)}$.

The existing small-signal model of the *S-S* compensated WPT system based on the EDF method has been derived in [28] and [29]. The state variables matrix is expressed as

$$\mathbf{x} = \begin{bmatrix} \hat{i}_{(1\mathrm{s})} & \hat{i}_{(1\mathrm{c})} & \hat{i}_{(2\mathrm{s})} & \hat{i}_{(2\mathrm{c})} & \hat{v}_{(1\mathrm{s})} & \hat{v}_{(1\mathrm{c})} & \hat{v}_{(2\mathrm{s})} & \hat{v}_{(2\mathrm{c})} & \hat{v}_{\mathrm{Co}} \end{bmatrix}^T. \quad (29)$$

The coefficients matrices corresponding to the standard EDF-based small-signal model in (10) and (11) are shown in (30a)–(30d) as follows:

$$\mathbf{B}_{\mathrm{ss}} = \begin{bmatrix} \frac{2m}{\pi L_{\mathrm{eq2}}}\sin\left(\frac{\pi}{m}D_{\mathrm{y}}\right) & \frac{2V_{\mathrm{in}}}{L_{\mathrm{eq2}}}\cos\left(\frac{\pi}{m}D_{\mathrm{y}}\right) & 0 \\ 0 & K_{14} & 0 \\ \frac{2m}{\pi L_{\mathrm{eqm}}}\sin\left(\frac{\pi}{m}D_{\mathrm{y}}\right) & \frac{2V_{\mathrm{in}}}{L_{\mathrm{eqm}}}\cos\left(\frac{\pi}{m}D_{\mathrm{y}}\right) & 0 \\ 0 & K_{15} & 0 \\ 0 & 0 & 0 \\ 0 & 0 & 0 \\ 0 & 0 & 0 \\ 0 & 0 & 0 \\ 0 & 0 & \frac{K_{18}}{C_{\mathrm{o}}} \end{bmatrix} \quad (30b)$$

$$\mathbf{C}_{\mathrm{ss}} = \begin{bmatrix} 0 & 0 & K_{16} & K_{17} & 0 & 0 & 0 & 0 & K_{18} \end{bmatrix} \quad (30c)$$

$$\mathbf{D}_{\mathrm{ss}} = \begin{bmatrix} 0 & 0 & R_{\mathrm{c}}K_{18} \end{bmatrix} \quad (30d)$$

$$\mathbf{A}_{\mathrm{ss}} = \begin{bmatrix} -\frac{R_1}{L_{\mathrm{eq2}}} & \Omega_{\mathrm{s}} & K_1 & K_2 & -\frac{1}{L_{\mathrm{eq2}}} & 0 & -\frac{1}{L_{\mathrm{eqm}}} & 0 & K_3 \\ -\Omega_{\mathrm{s}} & -\frac{R_1}{L_{\mathrm{eq2}}} & K_2 & K_4 & 0 & -\frac{1}{L_{\mathrm{eq2}}} & 0 & -\frac{1}{L_{\mathrm{eqm}}} & K_5 \\ -\frac{R_1}{L_{\mathrm{eqm}}} & 0 & K_6 & \Omega_{\mathrm{s}}+K_7 & -\frac{1}{L_{\mathrm{eqm}}} & 0 & -\frac{1}{L_{\mathrm{eq1}}} & 0 & K_8 \\ 0 & -\frac{R_1}{L_{\mathrm{eqm}}} & -\Omega_{\mathrm{s}}+K_7 & K_9 & 0 & -\frac{1}{L_{\mathrm{eqm}}} & 0 & -\frac{1}{L_{\mathrm{eq1}}} & K_{10} \\ \frac{1}{C_1} & 0 & 0 & 0 & 0 & \Omega_{\mathrm{s}} & 0 & 0 & 0 \\ 0 & \frac{1}{C_1} & 0 & 0 & -\Omega_{\mathrm{s}} & 0 & 0 & 0 & 0 \\ 0 & 0 & \frac{1}{C_2} & 0 & 0 & 0 & 0 & \Omega_{\mathrm{s}} & 0 \\ 0 & 0 & 0 & \frac{1}{C_2} & 0 & 0 & -\Omega_{\mathrm{s}} & 0 & 0 \\ 0 & 0 & K_{11} & K_{12} & 0 & 0 & 0 & 0 & K_{13} \end{bmatrix} \quad (30a)$$

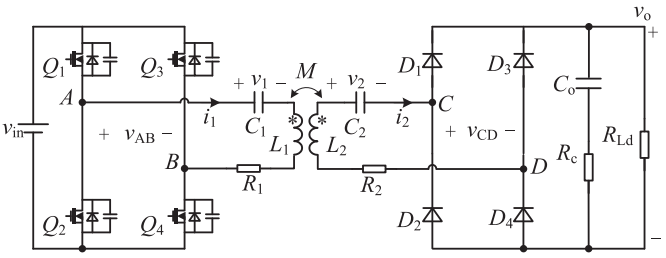

Fig. 7. Topology of the *S-S* compensated WPT system.

where $m = 1$ for half-bridge structure, and $m = 2$ for full-bridge structure, and

$$L_{\mathrm{eq1}} = L_2 - M^2/L_1 \tag{31a}$$

$$L_{\mathrm{eq2}} = L_1 - M^2/L_2 \tag{31b}$$

$$L_{\mathrm{eqm}} = L_1 L_2/M - M. \tag{31c}$$

K_1–K_{18} are the elements of the matrices $\mathbf{A}_{\mathrm{ss}}$–$\mathbf{D}_{\mathrm{ss}}$, as shown in Appendix B. As we have mentioned in Section V, the existing model and the proposed model share the same $\mathbf{A}_{\mathrm{ss}}$, $\mathbf{C}_{\mathrm{ss}}$, and $\mathbf{D}_{\mathrm{ss}}$, but have different $\mathbf{B}_{\mathrm{ss}}$. In the existing model, K_{14} and K_{15} of $\mathbf{B}_{\mathrm{ss}}$ are zero, but in the proposed model, they depend on $G_{\mathrm{AB(1c)}}$, i.e.,

$$K_{14} = \frac{G_{\mathrm{AB(1c)}}}{L_{\mathrm{eq2}}}, K_{15} = \frac{G_{\mathrm{AB(1c)}}}{L_{\mathrm{eqm}}}. \tag{32}$$

By substituting the expressions of $G_{\mathrm{AB(1c)}}$ in Tables I and II into (30b), the revised $\mathbf{B}_{\mathrm{ss}}$ is obtained. Substituting the $\mathbf{A}_{\mathrm{ss}}$–$\mathbf{D}_{\mathrm{ss}}$ into (12b), the modified expression of G_{vd} can be obtained.

An *S-S* compensated WPT system is designed in the laboratory. The circuit parameters are list in Table III. Fig. 8 shows the bode diagrams of G_{vd} for full-bridge *S-S* compensated WPT system by the existing model and the proposed model, where we can see that if D_{y} is small, the deviation between the existing model and the proposed model is small. However, as D_{y} increases to 1, the deviation gradually becomes large. This is because the absolute value of $G_{\mathrm{AB(1c)}}$ rises monotonically with D_{y} in the proposed model but remains zero in the existing model. Moreover, due to the opposite signs of $G_{\mathrm{AB(1c)}}$, there are a large distinction between the models for leading-leg PS and lagging-leg PS, especially in terms of phase curves. For the case in Fig. 8(c), the phase of leading-leg PS leads that of lagging-leg PS significantly, indicating the leading-leg PS is better in terms of the stability design in this case.

Fig. 9 shows the bode diagrams of $G_{\mathrm{vd}}(s)$ for the half-bridge *S-S* compensated WPT system by the existing model and the proposed model. It should be pointed out that in the existing model and the proposed model for dual-edge modulation, $G_{\mathrm{AB(1s)}}$ and $G_{\mathrm{AB(1c)}}$ are both zero when $D_{\mathrm{y}} = 0.5$ according to Table II, therefore $G_{\mathrm{vd}}(s) \equiv 0$ in the entire frequency range, indicating the duty-cycle perturbation has no effect on the output voltage. Due to this reason, the bode diagrams are not drawn in Fig. 9(b). From Fig. 9, we can see that if D_{y} is close to 0 or 1, the deviation between the existing model and the proposed model is small, but reaches the maximum when the duty-cycle reaches $D_{\mathrm{y}} = 0.5$, which coincides with the results in Table II. Besides, we can see that for the given *S-S* WPT system, when $D_{\mathrm{y}} < 0.5$, trailing-edge modulation is better than leading-edge modulation; when $D_{\mathrm{y}} > 0.5$, leading-edge modulation is better than trailing-edge modulation.

The following is to verify the effect of different duty-cycle control schemes on the stability of the closed-loop system. Fig. 10 is the corresponding closed-loop control block diagram of the full-bridge *S-S* WPT system, where H_{v} is the gain of the output voltage sensor, and V_{m} is the peak-peak value of the carrier wave of the pulsewidth modulator, whose value can be found in Table III. According to Fig. 10, the expression of the loop gain is

$$T(s) = \frac{H_{\mathrm{v}}}{V_{\mathrm{m}}} G_{\mathrm{c}}(s) G_{\mathrm{vd}}(s) \tag{33}$$

where the transfer function of the controller $G_{\mathrm{c}}(s)$ is designed as

$$G_{\mathrm{c}}(s) = \frac{9000}{s} \frac{s + 40000}{s + 5000}. \tag{34}$$

The expected output voltage is 20 V, which will be reached when the duty-cycle is 0.85. Based on the information above, the Bode plots of $T(s)$ for leading-leg PS control and lagging-leg PS control are collectively shown in Fig. 11, where we can find both control schemes share the same cut-off frequencies, namely 3 kHz, but the phase margins are different. According to the proposed model, the phase margin is 40° for leading-leg PS, but drops to −12° for lagging-leg PS, indicating the system should be stable in the former case, but unstable in the latter case. In contrast, the existing model predicts the phase margin to be 15° for both schemes, meaning the system should be stable in both cases. Obviously, the time-domain simulation waveforms given in Fig. 12 are completely consistent with the proposed model, verifying the value of the proposed model in control loop design and stability judgment.

VI. Experimental Verification

The prototype of the *S-S* compensated WPT system in Table III is built in the laboratory, photograph of which is shown in Fig. 13, where the digital signal processor (DSP) TMS320F280049C from Texas Instruments is used to implement all the duty-cycle control. Different carriers are obtained by changing the time-base counter mode of the enhanced pulsewidth modulator (ePWM) module of the DSP. To be specific, the up-count mode, down-count mode, and up-down-count mode of the time-base counter correspond to rising SC, falling SC, and TC. The vector network analyzer (VNA) Bode 100 is utilized to measure the bode diagrams of $G_{\mathrm{vd}}(s)$.

A. Measurement of $G_{vd}(s)$

The schematic diagram of the measurement of $G_{\mathrm{vd}}(s)$ is shown in Fig. 14, where the VNA first outputs a sine-sweep signal with a frequency range of 100 Hz to 125 kHz (the switching frequency). After isolated by the signal injector, the sine-sweep signal is superimposed with a dc voltage V_{dc} (V_{dc} is used to

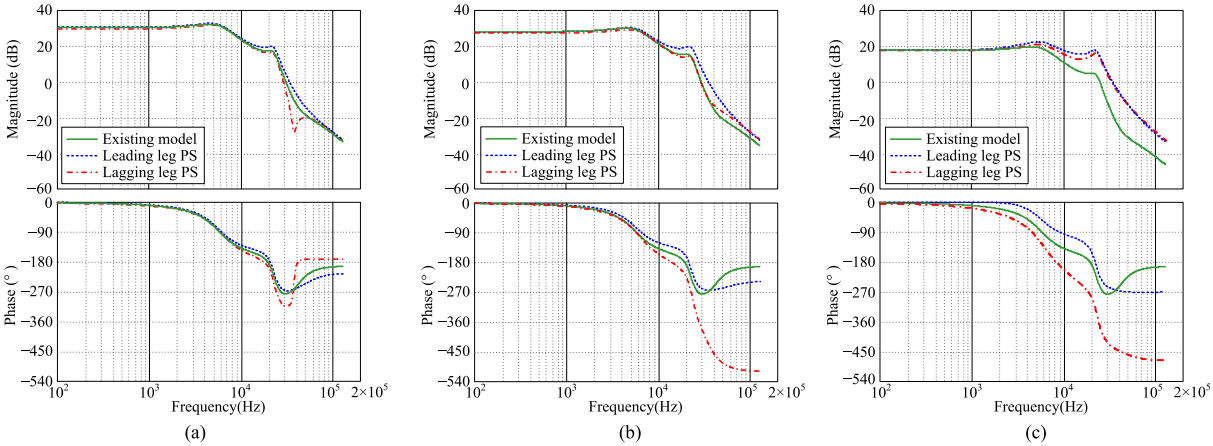

Fig. 8. Bode diagrams of G_{vd} of the full-bridge *S-S* WPT system by the existing model and the proposed models with different duty-cycles. (a) $D_{\mathrm{y}} = 0.25$. (b) $D_{\mathrm{y}} = 0.5$. (c) $D_{\mathrm{y}} = 0.85$.

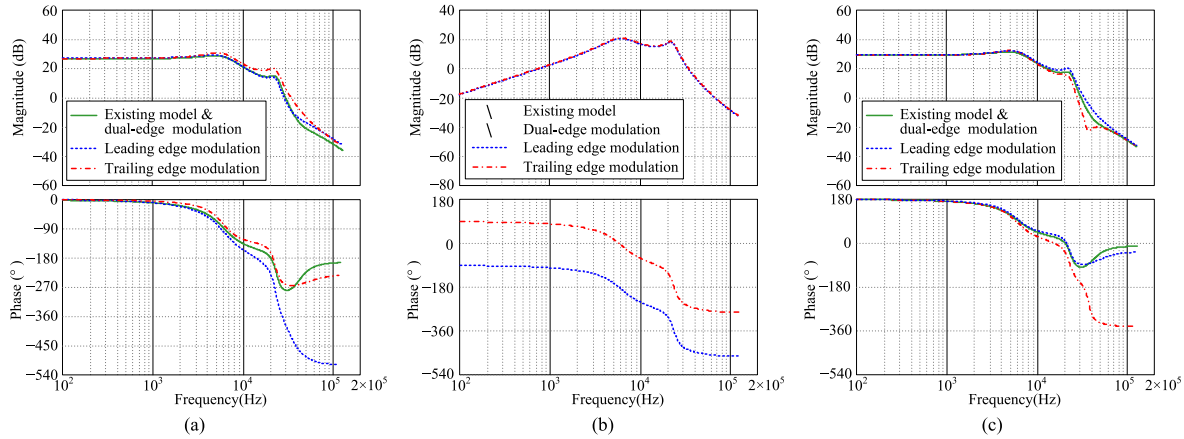

Fig. 9. Bode diagrams of G_{vd} of the half-bridge *S-S* WPT system by the existing models and the proposed models with different duty-cycles. (a) $D_{\mathrm{y}} = 0.25$. (b) $D_{\mathrm{y}} = 0.5$. (c) $D_{\mathrm{y}} = 0.85$.

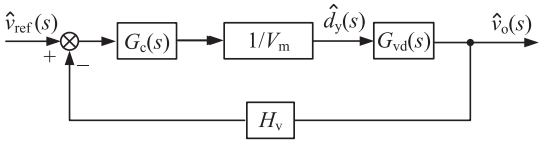

Fig. 10. Closed-loop control block diagram of the S-S WPT system.

regulate the steady-state duty-cycle) and then is converted to a digital value by the analog-to-digital converter module inside the DSP. The digital value compares with the time-base counter value in the ePWM module to generate a pair of complementary sinusoidally modulated pulse signals to drives the switches.

For full-bridge structure, two ePWM modules, e.g., ePWM1 and ePWM2 are applied since there are four active switches, namely Q_1–Q_4. As shown in Fig. 14, the two pairs of diagonal switches are Anded first. Their outputs are then ORed to obtain the actual duty-cycle d_{y}. The acquired waveforms of d_{y} and the output voltage v_{o}, are sent to VNA to draw the Bode plots.

For the half-bridge structure, only the ePWM1 module is used since there are only two switches Q_1–Q_2. Considering Q_1 is

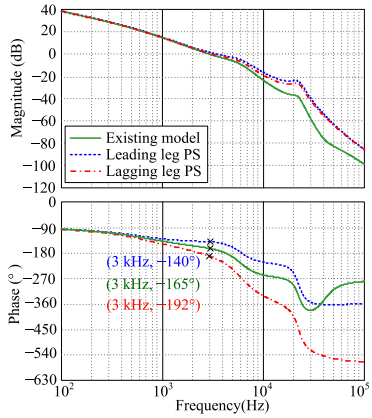

Fig. 11. Bode diagrams of the loop gain of the full-bridge *S-S* compensated WPT system using the existing model and the proposed model.

exactly the duty-cycle for the half-bridge structure, it is directly sent to the VNA without any logical operation.

Fig. 15 gives the measured $G_{\mathrm{vd}}(s)$ of the full-bridge *S-S* compensated WPT system. To maximize the difference between

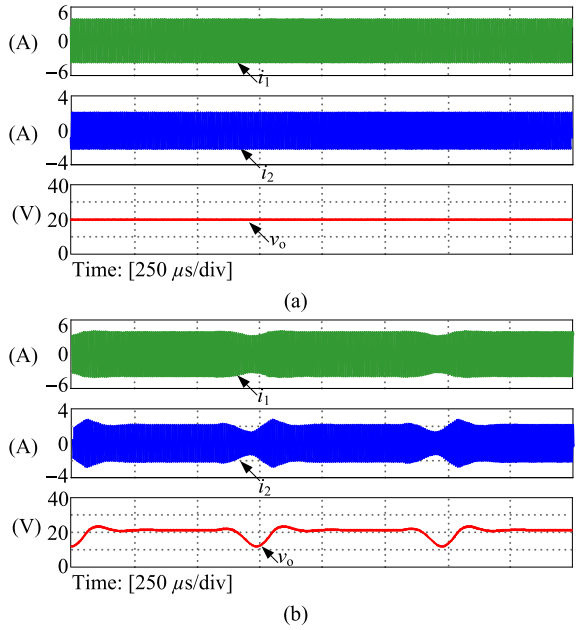

Fig. 12. Simulation waveforms of the closed-loop full-bridge S-S WPT system with different PS schemes. (a) Leading-edge PS. (b) Lagging-leg PS.

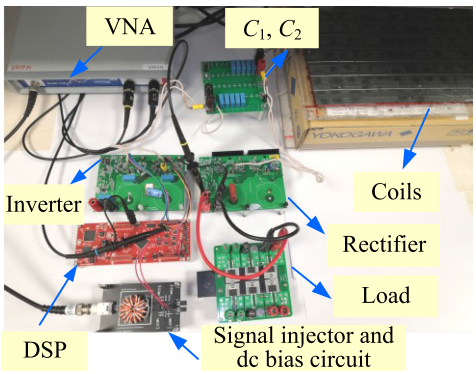

Fig. 13. Photograph of the *S-S* compensated WPT system prototype.

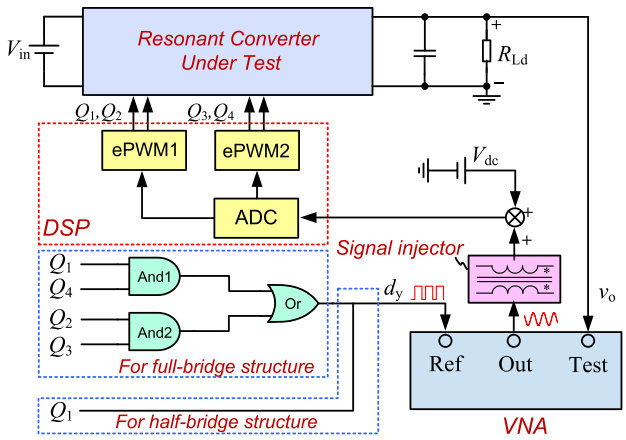

Fig. 14. Schematic diagram of the measurement circuit of $G_{\mathrm{vd}}(s)$.

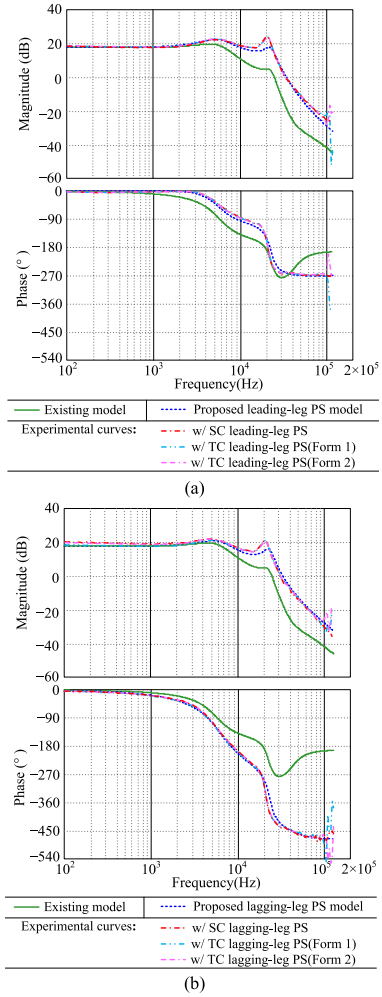

Fig. 15. Bode diagrams of G_{vd} of full-bridge *S-S* compensated WPT system by experiment and the proposed model when $D_{\mathrm{y}} = 0.85$ for (a) leading-leg PS and (b) lagging-leg PS.

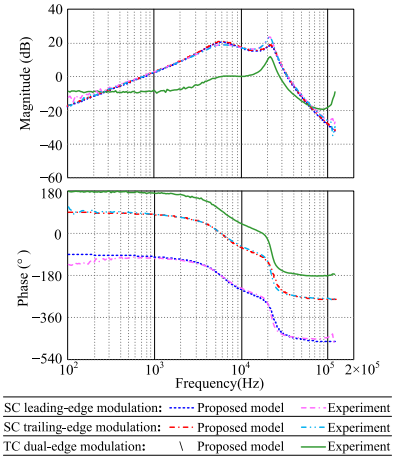

Fig. 16. Bode diagrams of G_{vd} of half-bridge *S-S* compensated WPT system by experiment and the proposed model when $D_{\mathrm{y}} = 0.5$ for various duty-cycle control schemes.

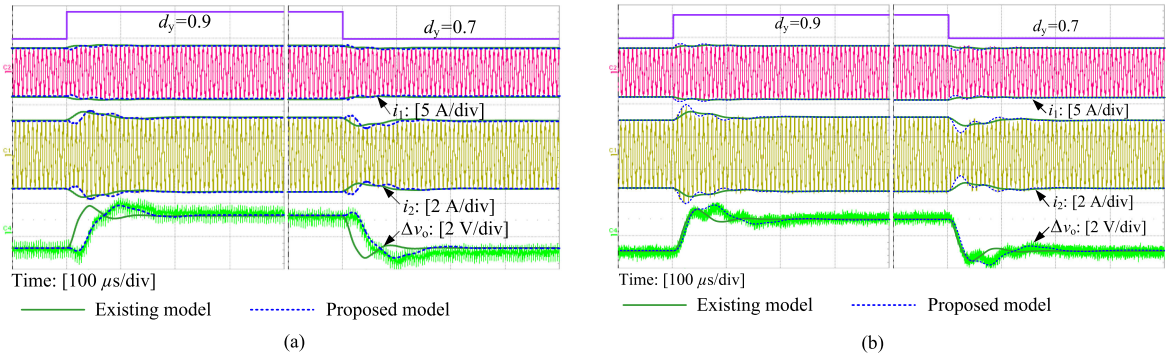

Fig. 17. Duty-cycle step response of the full-bridge *S-S* compensated WPT systems with different PS control schemes. (a) TC lagging-leg Form 1. (b) TC leading-leg Form 1.

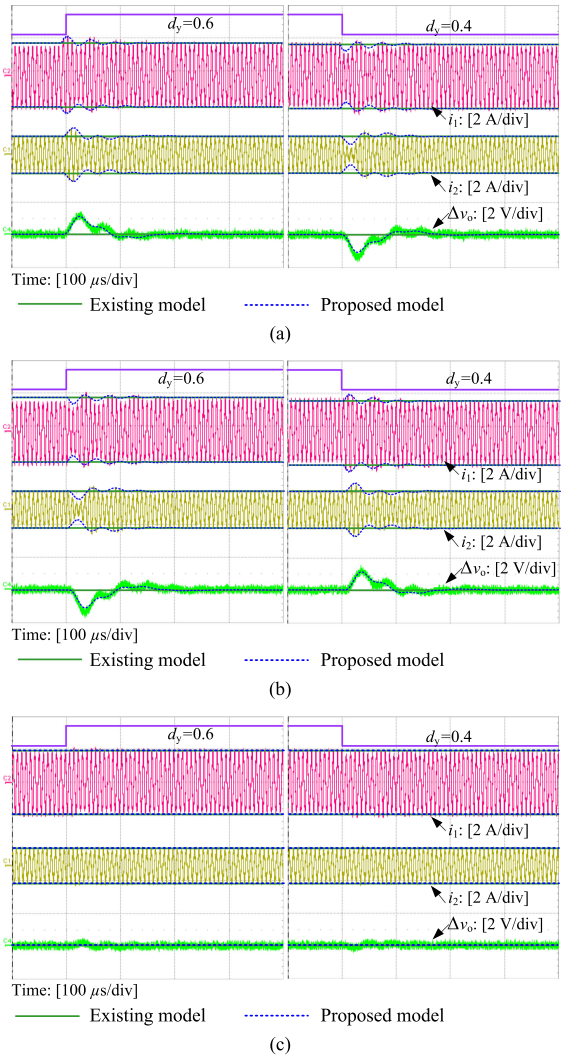

Fig. 18. Duty-cycle step response of the half-bridge *S-S* compensated WPT systems with different duty-cycle control schemes. (a) Trailing-edge modulation. (b) Leading-edge modulation. (c) Dual-edge modulation.

the existing model and the proposed models, the duty cycle should be as close to 1 as possible, which is chosen to be 0.85 here. Fig. 15(a) is the result when three kinds of leading-leg PS schemes are used. From Fig. 15(a), we can find that the measurement results of the three schemes are almost identical and all agree well with the proposed model. Similarly, the consistency of the proposed model and the measurement results with the lagging-leg PS scheme is also confirmed in Fig. 15(b).

Fig. 16 gives the experimental results of the half-bridge *S-S* compensated WPT system. D_y is set at 0.5 to maximize the difference between the existing model and the proposed models. According to Fig. 16, both the proposed leading-edge modulation model and trailing-edge modulation model agree well with the experimental curves. Besides, the measured magnitude curve for dual-edge modulation is not infinitesimal as the proposed model predicted, the deviation comes from the error of fundamental harmonic approximation. Despite the deviation, it still has a much smaller amplitude than those of leading-edge and trailing-edge modulation in a wide frequency range.

B. Step Response Predictions

To further verify the proposed model, the duty-cycle step response experiments under different duty-cycle control schemes are conducted.

Figs. 17 gives the experimental waveforms of the full-bridge *S-S* compensated WPT system as well as the prediction results by the existing model and the proposed model. From top to bottom, the waveforms in Fig. 17 are the duty-cycle, transmitting coil current i_1, receiving coil current i_2, and ac component of the output voltage Δv_o, respectively. The duty-cycle steps between 0.7 and 0.9. Fig. 17(a) and (b) correspond to TC lagging-leg PS Form 1 and TC leading-leg PS Form 1, respectively. Comparing Fig. 17(a) and (b), it can be readily found that the dynamic responses are quite different, showing the model of the system is highly dependent on the duty-cycle control schemes. Moreover, the predicted curves by the proposed model coincide very well with the experimental results in both cases, while these of the existing model fail to differentiate different duty-cycle control schemes and are found to deviate from the experimental results.

Similarly, the experimental results of the half-bridge *S-S* compensated WPT system are provided in Fig. 18, where Fig. 18(a)–(c) adopt the SC trailing-edge modulation, SC leading-edge modulation, and TC dual-edge modulations, respectively. The duty-cycle steps from 0.4 to 0.6. It can be found that the proposed model is capable of well tracking the transient experimental

waveforms in all cases. Besides, from Fig. 18(a) and (b), we can see that with the same duty cycle transient, the responses of the output voltage are reverse symmetrical. This can be interpreted with Fig. 9(b), where the trailing edge modulation and leading-edge modulation share exactly the same $G_{\rm vd}(s)$ magnitude, but the phase curve differs by 180° at the duty-cycle of 0.5. Conversely, the predicted curves by the existing model are all horizontal lines from Fig. 18(a)–(c). This is because when the duty-cycle is 0.5, $G_{\rm vd}(s) \equiv 0$ in the entire frequency range according to the existing model and the proposed model for dual-edge modulation, as discussed in Section V.

In general, the existing model is effective only for half-bridge resonant converters that adopt dual-edge modulation, but the proposed model is useful for both half-bridge and full-bridge resonant converters with various duty-cycle control schemes.

VII. Conclusion

Duty-cycle control is a widely used in resonant converters. However, the existing models of duty-cycle controlled resonant converters are found to deviate from the simulation and experiment results. The reason behind is investigated in this article, showing the zero-crossing instant change of the output voltage of the inverter caused by the duty-cycle perturbation should be taken into account while performing Fourier transform. Improved models of both full-bridge and half-bridge resonant converters are re-derived, which show that different duty-cycle control schemes lead to different phase curves of the duty-cycle-to-output-voltage transfer functions, thus care should be taken when selecting the duty-cycle control scheme for the adopted resonant topology to guarantee the stability. An *S-S* compensated WPT system is designed and fabricated to verify the validity of the proposed models.

Appendix A

This Appendix will extend the proposed EDF method-based modeling procedure to the GSSA method and DPT method.

As mentioned in Section I, the methodologies of the EDF method, GSSA method, and DPT method are to decompose the switching ripple of each variable in the resonant tank into two independent variables with dc operating points. However, the decomposition methods are different in some literature.

In the EDF-based model [21], [22], $v_{\rm AB}$ is separated into the sine and cosine terms

$$v_{\rm AB}(t) = \sum_{n=0}^{+\infty} \Big(v_{\rm AB(_{ns})} \sin(n\omega_{\rm s} t) + v_{\rm AB(_{nc})} \cos(n\omega_{\rm s} t) \Big). \tag{A1}$$

In the GSSA-based model [19], [20], $v_{\rm AB}$ is separated to the following form:

$$v_{\rm AB} = \sum_{n=0}^{+\infty} \left(\langle v_{\rm AB} \rangle_n e^{jn\omega_{\rm s} t} + \langle v_{\rm AB} \rangle_{-n} e^{-jn\omega_{\rm s} t} \right) \tag{A2}$$

where $\langle v_{\rm AB} \rangle_n$ and $\langle v_{\rm AB} \rangle_{-n}$ are conjugated. Separating $\langle v_{\rm AB} \rangle_n$ into the real part and imaginary part yields

$$\langle v_{\rm AB} \rangle_n = \langle v_{\rm AB} \rangle_n^{\rm r} + j \langle v_{\rm AB} \rangle_n^{\rm i}. \tag{A3}$$

$\langle v_{\rm AB} \rangle_n^{\rm r}$ and $\langle v_{\rm AB} \rangle_n^{\rm i}$ are the counterparts of $v_{\rm AB1s}$ and $v_{\rm AB1c}$. Substitution of (A3) into (A2) leads to

$$v_{\rm AB} = \sum_{n=0}^{+\infty} \Big(-2 \langle v_{\rm AB} \rangle_n^{\rm i}(t) \sin(\omega_{\rm s} t) + 2 \langle v_{\rm AB} \rangle_n^{\rm r}(t) cos(\omega_{\rm s} t) \Big). \tag{A4}$$

Comparing (A1) and (A4), it is obvious that

$$\langle v_{\rm AB} \rangle_n^{\rm i} = -\frac{1}{2} v_{\rm AB(ns)},\ \langle v_{\rm AB} \rangle_n^{\rm r} = \frac{1}{2} v_{\rm AB(nc)}. \tag{A5}$$

The gains from $\hat{d}_{\rm y}$to $\langle v_{\rm AB} \rangle_n^{\rm r}$ and $\langle v_{\rm AB} \rangle_n^{\rm i}$ are defined as $\langle G_{\rm AB} \rangle_n^{\rm r}$and $\langle G_{\rm AB} \rangle_n^{\rm i}$, respectively. According to (A5), the revised $\langle G_{\rm AB} \rangle_n^{\rm r}$and $\langle G_{\rm AB} \rangle_n^{\rm i}$ are solved to be

$$\langle G_{\rm AB} \rangle_n^{\rm r} = \frac{1}{2} G_{\rm AB(nc)},\ \langle G_{\rm AB} \rangle_n^{\rm i} = -\frac{1}{2} G_{\rm AB(ns)}. \tag{A6}$$

Since the expressions of $G_{\rm AB(ns)}$ and $G_{\rm AB(nc)}$ have been derived in this article, the proposed modeling procedure can be extended to GSSA method using (A6).

In the DPT based model [17], [18], $v_{\rm AB}$ is separated to be

$$v_{\rm AB} = \sum_{n=0}^{+\infty} \left({\rm Re} \left(v_{\rm AB(n)} e^{j\theta_{(n)}} e^{jn\omega_{\rm s} t} \right) \right) \tag{A7}$$

where $v_{\rm AB(n)} e^{j\theta_{(n)}}$ is a complex time-varying phasor. Separating it into the real part and imaginary part leads to

$$v_{\rm AB(n)} e^{j\theta_{(n)}} = v_{\rm AB(nr)} + j v_{\rm AB(ni)}. \tag{A8}$$

Substitution of (A8) into (A7) yields

$$v_{\rm AB} = \sum_{n=0}^{+\infty} \left({\rm Re} \left[\left(v_{\rm AB(nr)} + j v_{\rm AB(ni)} \right) e^{jn\omega_{\rm s} t} \right] \right). \tag{A9}$$

Comparing (A1) and (A9), the following relationship can be found

$$v_{\rm AB(nr)} = v_{\rm AB(nc)}, v_{\rm AB(ni)} = -v_{\rm AB(ns)}. \tag{A10}$$

Defining the gains from $\hat{d}_{\rm y}$to $v_{\rm AB(nr)}$and $v_{\rm AB(ni)}$ as $G_{\rm AB(nr)}$and $G_{\rm AB(ni)}$respectively, we have

$$G_{\rm AB(nr)} = G_{\rm AB(nc)}, G_{\rm AB(ni)} = -G_{\rm AB(ns)}. \tag{A11}$$

Based on (A11), the modeling procedure of this article can be readily extended to the DPT method.

Appendix B

This appendix gives the expressions of the elements in the matrices $\mathbf{A}_{\rm ss}$–$\mathbf{D}_{\rm ss}$ of the *S-S* compensated WPT system

$$K_1 = -\frac{R_2}{L_{\rm eqm}} - \frac{4 I_{\rm 2c}^2 V_{\rm Co}}{\pi L_{\rm eqm} I_{\rm pk}^3}, K_2 = \frac{4 I_{\rm 2s} I_{\rm 2c} V_{\rm Co}}{\pi L_{\rm eqm} I_{\rm pk}^3}$$

$$K_3 = -\frac{4 I_{\rm 2s}}{\pi L_{\rm eqm} I_{\rm pk}}, K_4 = -\frac{R_2}{L_{\rm eqm}} - \frac{4 I_{\rm 2s}^2 V_{\rm Co}}{\pi L_{\rm eqm} I_{\rm pk}^3}$$

$$K_5 = -\frac{4 I_{\rm 2c}}{\pi L_{\rm eqm} I_{\rm pk}}, K_6 = -\frac{R_2}{L_{\rm eq1}} - \frac{4 I_{\rm 2c}^2 V_{\rm Co}}{\pi L_{\rm eq1} I_{\rm pk}^3}$$

$$K_7 = \frac{4 I_{\rm 2s} I_{\rm 2c} V_{\rm Co}}{\pi L_{\rm eq1} I_{\rm pk}^3}, K_8 = -\frac{4 I_{\rm 2s}}{\pi L_{\rm eq1} I_{\rm pk}}$$

$$K_9 = -\frac{R_2}{L_{\mathrm{eq1}}} - \frac{4I_{2\mathrm{s}}^2 V_{\mathrm{Co}}}{\pi L_{\mathrm{eq1}} I_{\mathrm{pk}}^3}, K_{10} = -\frac{4I_{2\mathrm{c}}}{\pi L_{\mathrm{eq1}} I_{\mathrm{pk}}}$$
$$K_{11} = \frac{2}{\pi C_{\mathrm{o}}} \frac{R_{\mathrm{Ld}}}{R_{\mathrm{Ld}} + R_{\mathrm{c}}} \frac{I_{2\mathrm{s}}}{I_{\mathrm{pk}}}, K_{12} = \frac{2}{\pi C_{\mathrm{o}}} \frac{R_{\mathrm{Ld}}}{R_{\mathrm{Ld}} + R_{\mathrm{C}}} \frac{I_{2\mathrm{c}}}{I_{\mathrm{pk}}}$$
$$K_{13} = -\frac{1}{C_{\mathrm{o}}} \frac{1}{R_{\mathrm{Ld}} + R_{\mathrm{c}}}, K_{16} = \frac{2}{\pi C_{\mathrm{o}}} \frac{R_{\mathrm{Ld}} R_{\mathrm{c}}}{R_{\mathrm{Ld}} + R_{\mathrm{c}}} \frac{I_{2\mathrm{s}}}{I_{\mathrm{pk}}}$$
$$K_{17} = \frac{2}{\pi C_{\mathrm{o}}} \frac{R_{\mathrm{Ld}} R_{\mathrm{c}}}{R_{\mathrm{Ld}} + R_{\mathrm{c}}} \frac{I_{2\mathrm{c}}}{I_{\mathrm{pk}}}, K_{18} = \frac{R_{\mathrm{Ld}}}{R_{\mathrm{Ld}} + R_{\mathrm{c}}} \tag{A12}$$

where $I_{2\mathrm{s}}$, $I_{2\mathrm{c}}$, and I_{pk} are the coefficients of the sine part, cosine part, and peak value of i_2 in steady state, respectively.

REFERENCES

[1] E. Asa, K. Colak and D. Czarkowski, "Analysis of a novel interleaved CLL resonant converter for EV battery charger applications," in *Proc. IEEE Energy Convers. Congress Expo.*, 2014, pp. 2031–2036.

[2] J. Biela, U. Badstuebner, and J. W. Kolar, "Design of a 5-kW, 1-U, 10-kW/dm^3 resonant DC–DC converter for telecom applications," *IEEE Trans. Power Electron.*, vol. 24, no. 7, pp. 1701–1710, Jul. 2009.

[3] S. Saggini, S. Jiang, M. Ursino, and C. Nan, "A 99% efficient dual-phase resonant switched-capacitor-buck converter for 48 v data center bus conversions," in *Proc. IEEE Appl. Power Electron. Conf. Expo.*, 2019, pp. 482–487.

[4] M. Yaqoob, K. H. Loo, and Y. M. Lai, "Extension of soft-switching region of dual-active-bridge converter by a tunable resonant tank," *IEEE Trans. Power Electron.*, vol. 32, no. 12, pp. 9093–9104, Dec. 2017.

[5] Y. Zhang, Z. Yan, Z. Liang, S. Li, and C. C. Mi, "A high-power wireless charging system using LCL-N topology to achieve a compact and low-cost receiver," *IEEE Trans. Power Electron.*, vol. 35, no. 1, pp. 131–137, Jan. 2020.

[6] L. Shi, B. Liu, and S. Duan, "Burst-mode and phase-shift hybrid control method of LLC converters for wide output range applications," *IEEE Trans. Ind. Electron.*, vol. 67, no. 2, pp. 1013–1023, Feb. 2020.

[7] J.-H. Kim, C.-E. Kim, J.-K. Kim, J.-B. Lee, and G.-W. Moon, "Analysis on load-adaptive phase-shift control for high efficiency full-bridge LLC resonant converter under light-load conditions," *IEEE Trans. Power Electron.*, vol. 31, no. 7, pp. 4942–4955, Jul. 2016.

[8] Lo, C. L., M. Hsieh, and C. Lin, "Phase-shifted full-bridge series-resonant DC-DC converters for wide load variations," *IEEE Trans. Ind. Electron.*, vol. 58, no. 6, pp. 2572–2575, Jun. 2011.

[9] S. H. Ryu, D. H. Kim, M. J. Kim, J. S. Kim, and B. K. Lee, "Adjustable frequency-duty-cycle hybrid control strategy for full-bridge series resonant converters in electric vehicle chargers," *IEEE Trans. Ind. Electron.*, vol. 61, no. 10, pp. 5354–5362, Oct. 2014.

[10] Sun, Y. S., Y. Zhu, and X. Guo, "Interleaved boost-integrated LLC resonant converter with fixed-frequency PWM control for renewable energy generation applications," *IEEE Trans. Power Electron.*, vol. 30, no. 8, pp. 4312–4326, Aug. 2015.

[11] H. P. Park and J. H. Jung, "PWM and PFM hybrid control method for LLC resonant converters in high switching frequency operation," *IEEE Trans. Ind. Electron.*, vol. 64, no. 1, pp. 253–263, Jan. 2017.

[12] X. Li, X. Ruan, Q. Jin, M. Sha, and C. K. Tse, "Small-signal models with extended frequency range for dc-dc converters with large modulation ripple amplitude," *IEEE Trans. Power Electron.*, vol. 33, no. 9, pp. 8151–8163, Sep. 2018.

[13] M. G. Kim and M. J. Youn, "A discrete time domain modeling and analysis of controlled series resonant converter," *IEEE Trans. Ind. Electron.*, vol. 38, no. 1, pp. 32–40, Feb. 1991.

[14] J. Tang, S. Dong, C. Cui, and Q. Zhang, "Sampled-data modeling for wireless power transfer systems," *IEEE Trans. Power Electron.*, vol. 35, no. 3, pp. 3173–3182, Mar. 2020.

[15] K. Siri, I. Batarseh, and C. Lee, "Frequency response for the conventional parallel resonant converter based on the state-plane diagram," *IEEE Trans. Circuits Syst. I*, vol. 40, no. 1, pp. 33–42, Jan. 1993.

[16] Y. Hsieh and F. C. Lee, "Accurate small-signal modeling of resonant converter based on perturbation on the state plane," in *Proc. IEEE Energy Convers. Congress Expo.*, 2018, pp. 6809–6816.

[17] C. T. Rim and G. H. Cho, "Phasor transformation and its application to the dc/ac analyses of frequency phase-controlled series resonant converters (SRC)," *IEEE Trans. Power Electron.*, vol. 5, no. 2, pp. 201–211, Apr. 1990.

[18] H. Li, J. Fang, and Y. Tang, "Dynamic phasor-based reduced-order models of wireless power transfer systems," *IEEE Trans. Power Electron.*, vol. 34, no. 11, pp. 11361–11370, Nov. 2019.

[19] S. R. Sanders, J. M. Noworolski, X. Z. Liu, and G. C. Verghese, "Generalized averaging method for power conversion circuits," in *Proc. IEEE 21st Annu. Conf. Power Electron. Spec.*, 1990, pp. 333–340.

[20] S. R. Sanders, J. M. Noworolski, X. Z. Liu, and G. C. Verghese, "Generalized averaging method for power conversion circuits," *IEEE Trans. Power Electron.*, vol. 6, no. 2, pp. 251–259, Apr. 1991.

[21] E. X. Yang, F. C. Lee, and M. M. Jovanovic, "Small-signal modeling of series and parallel resonant converters," in *Proc. IEEE 7th Annu. Appl. Power Electron. Conf. Expo.*, 1992, pp. 785–792.

[22] A. Domínguez, A. Otín, L. A. Barragán, O. Lucía, and J. I. Artigas, "Thermal-electrical modeling and simulation of resonantly operated DC-DC converters based on extended describing function method," in *Proc. IEEE IECON*, 2012, pp. 5949–5954.

[23] S. Tian, F. C. Lee, and Q. Li, "A simplified equivalent circuit model of series resonant converter," *IEEE Trans. Power Electron.*, vol. 31, no. 5, pp. 3922–3931, May 2016.

[24] S. Tian, F. C. Lee, and Q. Li, "Equivalent circuit modeling of LLC resonant converter," *IEEE Trans. Power Electron.*, vol. 35, no. 8, pp. 8833–8845, Aug. 2020.

[25] L. Grajales and F. C. Lee, "Control system design and small-signal analysis of a phase-shift-controlled series-resonant inverter for induction heating," in *Proc. IEEE Power Electron. Spec. Conf.*, 1995, pp. 450–456.

[26] J. Tian, J. Petzoldt, T. Reimann, M. Scherf, and G. Berger G, "Envelope model of frequency-duty-controlled LLC converters," in *Proc. IEEE Power Electron. Spec. Conf.*, 2007, pp. 876–881.

[27] H. Feng, T. Cai, S. Duan, X. Zhang, and H. Hu, "Modeling and analysis of phase-shift controlled LCL resonant converter in wireless charging systems. in *Proc. IEEE Appl. Power Electron. Conf.*, 2017, pp. 3714–3719.

[28] Z. U. Zahid *et al.*, "Modeling and control of series-series compensated inductive power transfer system," *IEEE J. Emerg. Sel. Topics Power Electron.,* vol. 3, no. 1, pp. 111–123, Mar. 2015.

[29] Z. U. Zahid, Z. Dalala, and J.-S. J. Lai, "Small-signal modeling of series-series compensated induction power transfer system," in *Proc. IEEE Appl. Power Electron. Conf.*, 2014, pp. 2847–2853.

[30] B. Cheng, F. Musavi, and W. Dunford, "Novel small signal modeling and control of an LLC resonant converter," in *Proc. IEEE Appl. Power Electron. Conf.*, 2014, pp. 2828–2834.

[31] B. Yang, *Topology Investigation of Frontend DC/DC Converter For Distributed Power System*. Ph.D. dissertation, Virginia Polytechnic Inst. State Univ., Blacksburg, VA, USA, 2003.

[32] E. X. Yang, "Extended describing function method for small-signal modeling of resonant and multi-resonant converters," *Ph.D. dissertation, Dept. Elect. Comput. Eng., Virginia Tech.*, Blacksburg, VA, USA, Feb. 1994.

[33] L. Scandola, L. Corradini, and G. Spiazzi, "Small-signal modeling of uniformly sampled phase-shift modulators," *IEEE Trans. Power Electron.*, vol. 30, no. 10, pp. 5870–5880, Oct. 2015.

[34] L. Scandola, L. Corradini, and G. Spiazzi, "Multi-harmonic small-signal modeling of digitally controlled dc-dc series resonant converters," in *Proc. Control Model. Power Electron.,* 2015, pp. 1–8.

[35] X. Li and X. Ruan, "A generic and accurate frequency-domain model for buck, boost and buck-boost converters," in *Proc. IEEE Energy Convers. Congress Expo.*, 2014, pp. 3760–3766.

[36] Y. Jiang, X. Ruan, C. Xiong, and X. Ruan, "Study of loop gain measurement of digitally controlled dc/dc converters," in *Proc. IEEE 8th Int. Power Electron. Motion Control Conf.*, 2016, pp. 2806–2812.

Xin Li (Member, IEEE) received the B.S. and Ph.D. degrees in electrical engineering and automation from Nanjing University of Aeronautics and Astronautics, Nanjing, China, in 2012 and 2018, respectively.

In 2019, he worked as a Research Engineer with Huawei Technologies Co., Ltd., Shanghai, China. Since 2020, he has been a Research Fellow with Nanyang Technological University, Singapore. His current research interests include modeling, control and design of PWM converter, resonant converter, and wireless power transfer system.

Yiming Zhang (Member, IEEE) received the B.S. and Ph.D. degrees in electrical engineering from Tsinghua University, Beijing, China, in 2011 and 2016, respectively.

From 2017 to 2019, he was a Postdoctoral Researcher with San Diego State University, San Diego, CA, USA. Since August 2019, he has been a Research Fellow with Nanyang Technological University, Singapore. He has authored one book from Springer, authored or coauthored more than 60 technical papers in journals and conference proceedings. His research interests include wireless power transfer for electric vehicles and mobile phones, and resonant converters.

Dr. Zhang was the recipient of the Outstanding Doctoral Dissertations of Tsinghua University, in 2016. He was recognized as an Outstanding Reviewer for the IEEE TRANSACTIONS ON POWER ELECTRONICS in 2019. He has been a Topic Chair for IEEE Transportation Electrification Conference and Exposition in 2018.

Shuxin Chen (Student Member, IEEE) received the B.Eng. degree in electronic engineering from the Hong Kong Polytechnic University, Hong Kong, in 2015, the bachelor's degree in microelectronic engineering from the Sun Yet-sen University, Guangzhou, China, in 2015, and the M.Sc. degree in power engineering, in 2016, from Nanyang Technological University, Singapore, where he is currently working toward the Ph.D. degree in electrical and electronic engineering.

From 2018 to 2019, he was a Visiting Scholar with the Future Energy Electronics Center, Virginia Tech, VA, USA. His current research interests include wireless power transfer and power converter control.

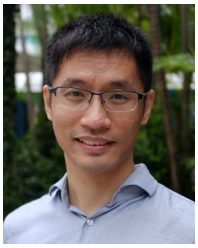

Xin Zhang (Senior Member, IEEE) received the Ph.D. degree in electronic and electrical engineering from Nanjing University of Aeronautics and Astronautics, Nanjing, China, in 2014, and the Ph.D. degree in automatic control and systems engineering from the University of Sheffield, Sheffield, U.K., in 2016.

From February 2014 to December 2016, he was a Research Associate with The University of Sheffield. From January 2017 to September 2017, he was a Research Fellow with the City University of Hong Kong, Hong Kong. From September 2017 to August 2020, he was an Assistant Professor with Nanyang Technological University. He is currently a Professor with Zhejiang University, Hangzhou, China. He has authored or coauthored more than 100 SCI journal papers and held about 10 patents, as well as four Springer books. His research interests include power electronics, power systems, and advanced control theory, together with their applications in various sectors.

Dr. Zhang was the recipient of the Highly Prestigious Chinese National Award for Outstanding Students Abroad in 2016. He is the Associated Editor of many international top journals, such as IEEE TRANSACTIONS ON INDUSTRIAL ELECTRONICS, IEEE JOURNAL OF EMERGING AND SELECTED TOPICS IN POWER ELECTRONICS, IEEE OPEN JOURNAL OF POWER ELECTRONICS, IEEE ACCESS, IET POWER ELECTRONICS, *China Electrotechnical Society Transactions on Electrical Machines and Systems*, etc.

Yi Tang (Senior Member, IEEE) received the B.Eng. degree in electrical engineering from Wuhan University, Wuhan, China, in 2007, and the M.Sc. and Ph.D. degrees in electrical and electronic engineering from the School of Electrical and Electronic Engineering, Nanyang Technological University, Singapore, in 2008 and 2011, respectively.

From 2011 to 2013, he was a Senior Application Engineer with Infineon Technologies Asia Pacific, Singapore. From 2013 to 2015, he was a Postdoctoral Research Fellow with Aalborg University, Aalborg, Denmark. Since March 2015, he has been with Nanyang Technological University, Singapore, where he is currently an Associate Professor. He is the Cluster Director of the Advanced Power Electronics Research Program with the Energy Research Institute, Nanyang Technological University.

Dr. Tang was the recipient of the Infineon Top Inventor Award in 2012, the Early Career Teaching Excellence Award in 2017, and four IEEE Prize Paper Awards. He is an Associate Editor for the IEEE TRANSACTIONS ON POWER ELECTRONICS and the IEEE JOURNAL OF EMERGING AND SELECTED TOPICS IN POWER ELECTRONICS.